

ARTICLE OPEN



Thermoplastic elastomer enhanced interface adhesion and bending durability for flexible organic solar cells

Zihan Xu^{1,2,3}, Yunfei Han^{1,2,3}, Yuanyuan Bai³, Xingze Chen^{1,2,3}, Jingbo Guo^{1,2,3}, Lianping Zhang^{2,3}, Chao Gong^{2,3}, Qun Luo^{1,2,3}, Ting Zhang^{1,3} and Chang-Qi Ma^{1,2,3}

Stable interface adhesion and bending durability of flexible organic solar cells (FOSCs) is a basic requirement for its real application in wearable electronics. Unfortunately, the device performance always degraded during continuous bending. Here, we revealed the weak interface adhesion force between MoO₃ hole transporting layer (HTL) and the organic photoactive layer was the main reason of poor bending durability. The insertion of an interface bonding layer with a thermoplastic elastomer, polystyrene-block-poly(ethylene-ran-butylene)-block-polystyrene (SEBS) effectively improved the interface adhesion force of MoO₃ HTL and the active layer and decreased the modulus, which ensured higher than 90% of the initial efficiency remaining after 10000 bending. Meanwhile, the FOSCs gave an efficiency of 14.18% and 16.15% for the PM6:Y6 and PM6:L8-BO devices, which was among the highest performance of FOSCs. These results demonstrated the potential of improving the mechanical durability of FOSCs through thermoplastic elastomer interface modification.

npj Flexible Electronics (2022)6:56; <https://doi.org/10.1038/s41528-022-00188-2>

INTRODUCTION

Recently, with the rapid development of flexible electronics, a variety of wearable electronic devices have gradually entered our lives, such as biosensors¹, electronic skins², etc. The power consumption of these devices is generally about 100–10 mW³. At present, these devices are mostly powered by flexible batteries or micro-supercapacitors⁴. But, frequent charging or replacement of batteries is not convenient and will affect the service life of devices. Therefore, it is urgent to develop renewable energy technology to replace conventional batteries. Flexible organic solar cells (FOSCs) are regarded as good choices for wearable energy harvest due to their features of flexible⁵, light weight⁶, patternable⁷, and high optical response under indoor light^{8,9}. In recent years, due to the innovation of organic donors, acceptors^{10–13}, and interlayer materials^{14,15}, and the development of device fabrication technology^{16–18}, the performance of FOSCs has improved rapidly^{18–23}. Currently, both the efficiency of single FOSCs^{18,22–25} and large-area modules²⁶ have achieved great developments. Meanwhile, high-performance ultrathin flexible OSCs has been integrated with sensor to detect physiological signal, which can be attached to skins²⁷ or textiles²⁸. For the future real application of FOSCs, besides device efficiency and long-term stability, reasonable mechanical properties are also crucial.

Regarding flexible electronics, mechanical properties, including bending resistance, stretch properties, and distortion resistance are typical evaluation parameters²⁹. To improve the mechanical properties of FOSCs, researchers have developed systematic approaches to optimize and modify the flexible electrode^{30–39}, electron transporting layer (ETL)^{26,40–43}, and active layer^{44–51}, which enabled improved mechanical properties. On the side of the flexible electrode, Chen et al. prepared a high-quality flexible conductive electrode (called FlexAgNE) by adding poly (sodium 4-styrenesulfonate) (PSSNa) polyelectrolyte in AgNWs dispersion³⁰. The FOSCs based on FlexAgNE electrodes have high flexible

durability thanks to the tight bonding force between polyethylene terephthalate and (PET) substrates, as well as the interaction of ZnO NPs and PSSNa³¹. Tang et al. imitated the internal structure of leaves and prepared a composite electrode contained polyimide (PI), polystyrene spheres, ZnO, and AgNWs with high optical and mechanical properties³². Similarly, Kim et al. obtained a composite electrode with high mechanical properties by completely embedding conductive polymer and AgNWs in colorless polyimide substrate⁵². Some simple methods like hot pressing³⁵, and cold isostatic pressure³⁹ were used to increase the network connection of AgNWs. Modifying AgNWs with conductive materials such as graphene oxide³⁶, MXene³⁷, PH1000³⁸, InSnTiO⁵³, and Al-doped ZnO⁴³ could passivate AgNWs, avoid performance degradation, and weld AgNWs. Regarding ETL, Zhou et al. reported a strategy that chelated Zn²⁺ with polyethylenimine (PEI) (called PEI-Zn)⁴¹, which not only improved the bending resistance ability of ETL, but also enhanced adhesion between the electron transporting layer (ETL) and active layer, and ultimately improved the mechanical stability of OSCs. Similarly, Chen et al. improved the mechanical stability of ETL and its adhesion force to the active layer by adding polydopamine (PDA) to zinc oxide⁴².

In term of the organic photoactive layer, doping suitable third component in the organic photoactive layer is considered to be a feasible strategy to improve the mechanical stability of the films and devices^{54,55}. The insulating polymer could form an insulating matrix in the doped active layer and improve the flexibility of OSCs^{44,45}. Till now, polyolefin elastomer (POE)⁴⁶, polystyrene-block-poly(ethylene-ran-butylene)-block-polystyrene (SEBS)⁴⁷, N2200⁵¹, etc. have been used as the additive of the active layer. Although many efforts were made to improve the mechanical property through various material optimization approaches, the underlying reason for device degradation during bending is not been systematically studied yet. Besides, most of the preliminary works focused on the bending durability of materials itself. Since OSC is a

¹School of Nano-Tech and Nano-Bionics, University of Science and Technology of China, Hefei, PR China. ²Printable Electronics Research Center, Suzhou Institute of Nano-Tech and Nano-Bionics, Chinese Academy of Sciences, Suzhou, PR China. ³i-Lab, Suzhou Institute of Nano-Tech and Nano-Bionics, Chinese Academy of Sciences, Suzhou, PR China. ✉email: qluo2011@sinano.ac.cn; tzhang2009@sinano.ac.cn; cqma2011@sinano.ac.cn

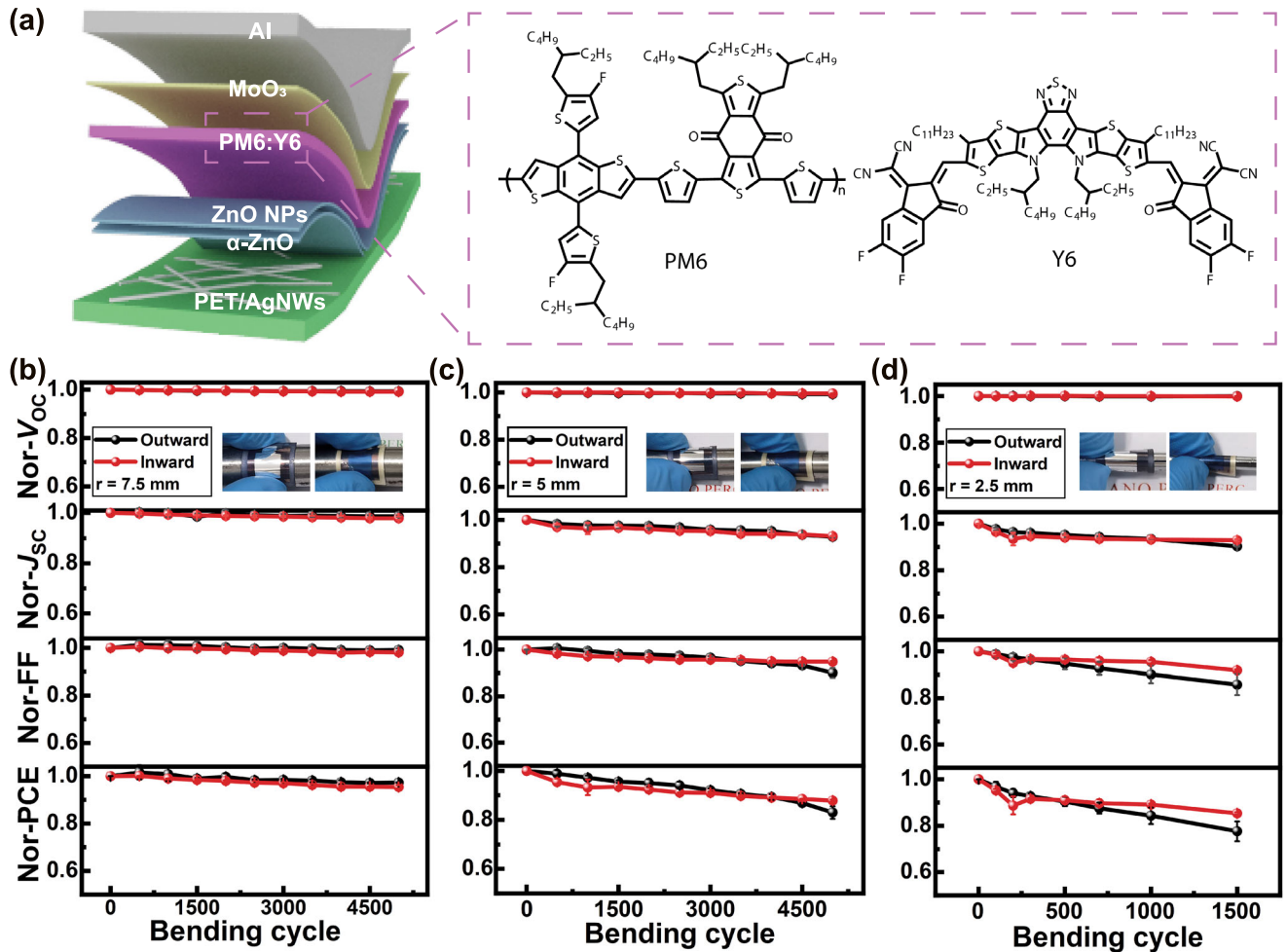


Fig. 1 Bending durability of inverted FOSCs. **a** Device structure and molecular structures of PM6 and Y6. Evolution of V_{OC} , J_{SC} , FF, and PCE of the FOSCs during continuous bending in inward and outward direction with bending radii of **b** 7.5, **c** 5.0, and **d** 2.5 mm.

typical device with a sandwich structure, it is predictably that the mechanical property of the interfaces between different functional layers would also significantly impact the bending resistance⁵⁶. Whereas, rare work investigated the relationship between interface adhesion and device bending resistance.

In this work, the degradation mechanism of flexible organic solar cells (FOSCs) during bending was systematically studied and the main reason was revealed. We firstly demonstrated the performance decrease was mainly due to the destruction of MoO₃ due to poor interface adhesion between the MoO₃ hole transporting layer (HTL) and the organic photoactive layers. An interface treating strategy to improve the interface adhesion force between MoO₃ and the active layer was developed through doping SEBS in the photoactive layer or modifying the active layer with SEBS. The dramatically increased interface adhesion through using SEBS as interface bonding layer pushed the improvement of device bending durability, with 95% and 91% of initial efficiency remaining after 5000 and 10000 times bending with a bend radius of 5 mm. Meanwhile, high performance was maintained for the SEBS modified device, and an efficiency of over 16% that among the highest performance of FOSCs was achieved.

RESULT AND DISCUSSION

Degradation trend and the reason

First of all, we investigated the performance evolution of FOSCs during bending. 0.64 cm² FOSCs with an inverted structure of

PET/AgNWs/ α -ZnO/ZnO NPs/active layer heterojunction (BHJ)/MoO₃/Al were fabricated according to previous work^{57,58}. Here, PM6:Y6 heterojunction with PM6 as electron donor and Y6 as electron acceptor was used as the active layer. α -ZnO and ZnO NPs were amorphous ZnO and ZnO nanoparticles layer, respectively. The flexible substrate was 125 μ m thick. The device structure and molecular structures are shown in Fig. 1a. An optimized champion PCE of 14.83% was achieved for the 0.64 cm² PM6:Y6 FOSCs, which was one of the highest values among the AgNWs-based FOSCs^{41,58–60}.

The mechanical flexibility of FOSCs during bending in both outward and inward directions at different bending radii was exhibited in Fig. 1b. After 5000 continuous bending cycles, the PET/AgNWs FOSCs showed good mechanical flexibility as the bending radius was 7.5 mm, maintaining higher than 95% of initial PCEs. As the radius decreased to 5 mm, 88% and 81% of initial PCEs remained in inward and outward bending directions, respectively. Similar results were observed during bending with a radius of 2.5 mm. After 1500 bending cycles, only 85% and 75% of initial PCE were retained for the inward and outward bending. In all, in comparison with bending in the inward direction, the device in outward bending showed more obvious damage, implying device degradation is more serious when the device suffered from tensile stress rather than compression stress, which was similar to the previous reports^{61,62}. In addition, we can find that both during inward or outward bending, the decline of short circuit current density (J_{SC}) and fill factor (FF) took responsibility

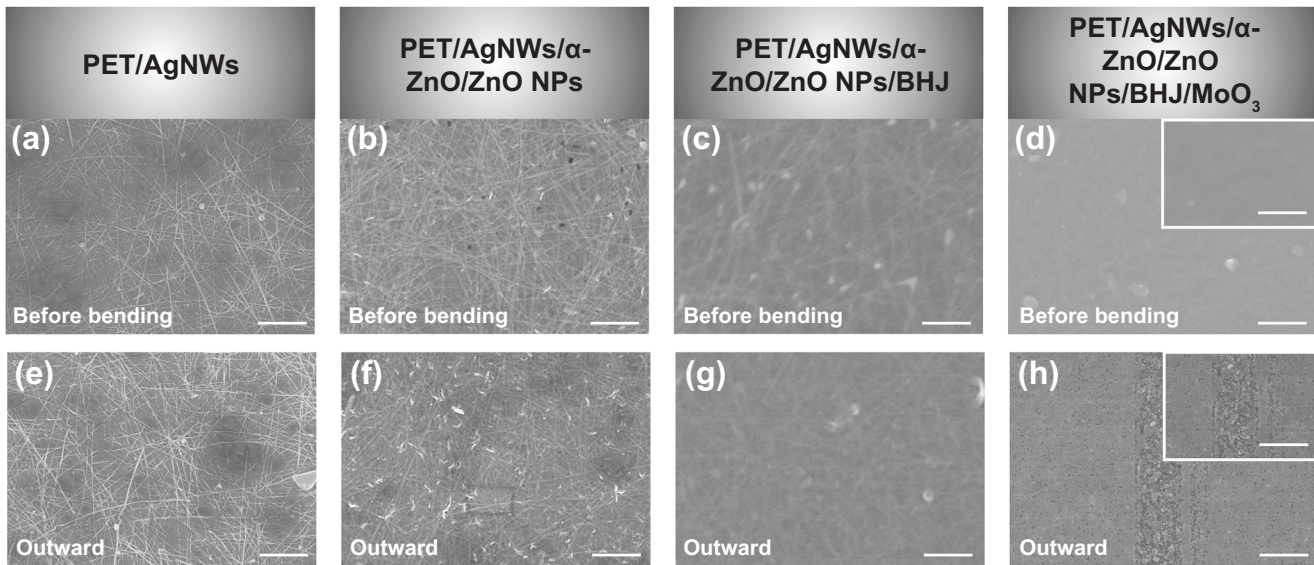


Fig. 2 Surface morphologies of FOSC films before and after bending. SEM images of **a, e** PET/AgNWs film, **b, f** PET/AgNWs/ α -ZnO/ZnO NPs film, **c, g** PET/AgNWs/ α -ZnO/ZnO NPs/BHJ film, **d, h** PET/AgNWs/ α -ZnO/ZnO NPs/BHJ/MoO₃ film before and after 1000 outward bending cycles with a radius of 5 mm. The scale bar is 2 μ m. Insets show the magnified SEM images. The scale bar of insets is 1 μ m.

for performance decrease, while open circuit voltage (V_{OC}) almost retained constant during bending. Take outward bending with a radius of 5 mm for instance, J_{SC} and FF were reduced by 7.4% and 11.5%, respectively. With the bending radius decreased to 2.5 mm, loss of FF was more obvious than J_{SC} . Specifically, J_{SC} was reduced by 9.4% and FF was reduced by 17.4% respectively. The corresponding J - V characteristics and performance parameters before and after bending were summarized in Supplementary Table 1. It was demonstrated that series resistance (R_s) slightly increased, and shunt resistance (R_{sh}) dramatically decreased after bending, which illustrated that the interface contact became worse⁶³. In addition, Electrochemical Impedance Spectroscopy (EIS) (Supplementary Fig. 1, Supplementary Table 2) showed the devices after bending had higher transporting resistance (406.8 Ω) than that of the pristine device (24.5 Ω). Although the interface contact became worse, the energy level alignment of the device did not change, which made V_{OC} keeping stable.

To further understand the origin of performance decay for these AgNWs electrode-based OSCs, the individual functional layers and the whole devices were bent for 1000 cycles with a bending radius of 5 mm, and the SEM images of these films before and after bending were investigated and shown in Fig. 2. As shown in Fig. 2a–c and Supplementary Fig. 2a–c, negligible change was observed for PET/AgNWs electrode, PET/AgNWs/ α -ZnO/ZnO NPs, and PET/AgNWs/ α -ZnO/ZnO NPs/BHJ (PM6:Y6) films after 1000 cycles bending, implying these functional layers offered superior mechanical robustness during bending. However, obvious fractures and exfoliation were observed in the MoO₃ films after 1000 cycles (Fig. 2h). Meanwhile, cracks in Al electrode were found in the optical microscope photographs and SEM images of the complete flexible devices and shown in Supplementary Fig. 2. A similar phenomenon of MoO₃ exfoliation was found in the case of inward bending, but the damage of MoO₃ and Al was much milder (Supplementary Fig. 3). Some researchers confirmed that the performance degradation of flexible devices with multilayers structure under stress was mainly caused by the expansion of films micro-cracks, which further caused the formation of large crack and films peeling⁶². The poor adhesion has been regarded as a basic reason. To further prove the failure mechanism during bending, PET/AgNWs, PET/AgNWs/ α -ZnO/ZnO NPs, PET/AgNWs/ α -ZnO/ZnO NPs/PM6:Y6, and PET/AgNWs/ α -ZnO/ZnO NPs/PM6:Y6/MoO₃ films were pre-bended for 1000 cycles in prior to the

fabrication of FOSCs. The corresponding devices named pre-AgNWs, pre-ZnO, pre-BHJ, and pre-MoO₃ OSCs stood the devices with pre-bended AgNWs, pre-bended AgNWs/ α -ZnO/ZnO NPs, pre-bended AgNWs/ α -ZnO/ZnO NPs/PM6:Y6, and pre-bended AgNWs/ α -ZnO/ZnO NPs/PM6:Y6/MoO₃ films, respectively. The device performance parameters were summarized in Supplementary Table 3. In comparison with standard FOSCs, the pre-AgNWs, pre-ZnO, and pre-BHJ OSCs showed similar device performance. On contrary, pre-MoO₃ OSCs were short-circuited. This result was similar to the devices with half-covered MoO₃ HTL (Supplementary Fig. 4), in which only half of the active layers were covered by MoO₃ layer. These results definitely proved the destruction of the MoO₃ layer is responsible for the mechanical invalidation of FOSCs. Specifically, breakage or even exfoliation of the MoO₃ layer caused poor interface contact and large transfer resistance between MoO₃ and the active layer, resulting in a deadly decrease in device performance.

Interface adhesion enhancement through introducing SEBS at the interface of MoO₃ and active layer

As discussed above, the poor adhesion of MoO₃ with the organic photoactive layer resulted in exfoliation of MoO₃ and Al electrode during continuous bending cycles, therefore the enhancement of interface adhesion force between MoO₃ and active layer could be a possible strategy to improve the mechanical properties. To improve the adhesion between MoO₃ and the active layer, and reduce the occurrence of cracks in MoO₃, a thermoplastic elastomer with good adhesion and mechanical properties, styrene-ethylene-butylene-styrene copolymer (SEBS, Fig. 3a), was selected as a bonding layer of the active layer and MoO₃ in this work. SEBS has been widely used as a flexible substrate material in flexible electronics, which has good flexibility^{64–67}. Herein, SEBS was doped in the organic photoactive layers or deposited on the top of active layers as an interface layer underneath the MoO₃ HTL (Fig. 3b). The adhesion force between MoO₃ and active layer films in these devices was evaluated by 3M tape peeling experiment (Fig. 3c–e and Supplementary Fig. 5). As exhibited in Fig. 3c, the Al top electrode together with MoO₃ films (proved by the XPS results, *vide infra*) was easily detached by 3M tape for the devices without SEBS due to the weak adhesion between the active layer and MoO₃. For the SEBS doped or SEBS interface

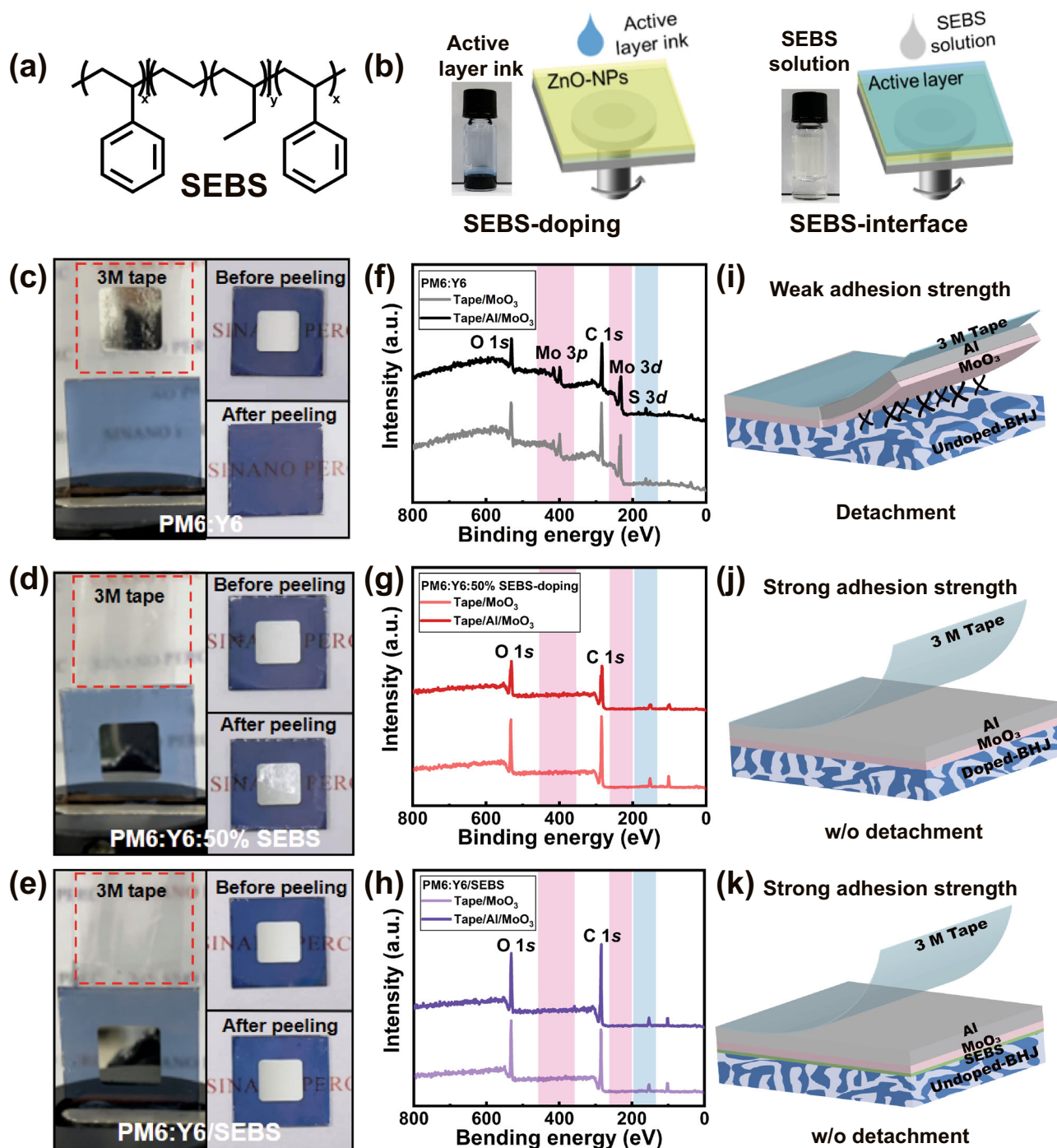


Fig. 3 Qualitative characterization of adhesion improvement. **a** Molecular structure of SEBS, **b** Schematic diagram of SEBS-doping and SEBS-interface strategies. Photographs of 3 M tape peeling measurement: **c** PM6:Y6 **d** PM6:Y6:50%SEBS, and **e** PM6:Y6/SEBS (8 mg mL^{-1}). XPS spectra of the remained materials on the tapes that peeled from the **f** PM6:Y6, **g** PM6:Y6:50% SEBS, and **h** PM6:Y6/SEBS (8 mg mL^{-1}). **i–k** Schematic diagram of the 3 M tape peeling measurement.

modified active layer with a low concentration, the Al electrode and MoO_3 HTL were still peeled by 3 M tape (Supplementary Fig. 5a, b, d, e). However, as the doping concentration or modification concentration increased to 50–100% or 8–12 mg mL^{-1} , the MoO_3 HTL and Al electrode kept unchanged. The interface adhesion was also accessed through cross-cut measurement, and the results were shown in Supplementary Fig. 6. We found MoO_3 and the top electrodes were totally peeled off from the active layer for the pristine and 30% SEBS-doping devices. For the PM6:Y6:50% SEBS and PM6:Y6/SEBS involved devices, more than 50% and 70%

of the films were retained after 3 M tape peeling. According to the industrial standard^{68,69}, the adhesion force level was 0 (0 or 30% SEBS doping), 2B (PM6:Y6:50%SEBS), and 3B (PM6:Y6/SEBS), respectively.

The materials that peeled off from MoO_3 and MoO_3/Al films by 3 M tapes were characterized by X-ray photoelectron spectroscopy (XPS). Both for the PM6:Y6/ MoO_3 and the PM6:Y6/ MoO_3/Al films without SEBS (Fig. 3f), we could obviously find peaks from core level of Mo 3d and Mo 3p that belonged to MoO_3 and S 3d peaks attributed to the active layer, suggesting both MoO_3 and partial of

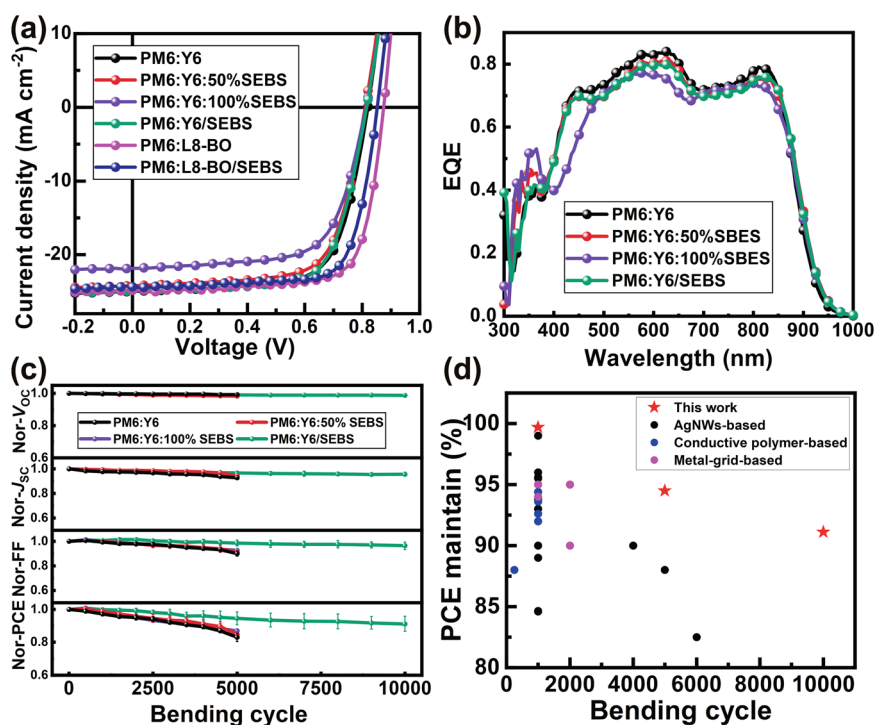


Fig. 4 Device performance. **a** J - V characteristics and **b** EQE spectra of SEBS treated devices. **c** Evolution of V_{OC} , J_{SC} , FF, and PCE after 5000 outward bending cycles with a radius of 5 mm for the PM6:Y6, PM6:Y6:50% SEBS, PM6:Y6:100%SEBS, and PM6:Y6/SEBS films-based flexible devices. **d** Summary of bending durability of the FOSCs.

organic photoactive layers have been exfoliated. In contrast, neither core level of Mo $3d/3p$ nor S $3d$ was detected in the SEBS-doping and SEBS interface-based devices. Such a result strongly proved the adhesion between the active layer and MoO_3/Al was significantly improved (Fig. 3j, k) after the introduction of SEBS. Then, the PM6:Y6:50%SEBS/ MoO_3 and PM6:Y6/SEBS/ MoO_3 films were also pre-bended for 1000 times with bending radius of 5 mm. After 1000 pre-bending cycles, the Al top electrode was deposited on these films to form a complete device. As shown in Supplementary Table 4, these devices still presented a similar device performance as the device with fresh BHJ/ MoO_3 films. This observation undoubtedly proved the SEBS-involved films could sustain repeated mechanical bending. Figure 3i-k shows the schematic diagram of different interface adhesion force for the pristine films and SBSB-involved films.

Improved bending resistance of FOSCs

To investigate the effect of SEBS-doping and SEBS-interface strategies on the performance of FOSCs, FOSCs devices with an area of 0.64 cm^2 based on inverted structure were fabricated. The J - V characteristics and EQE spectra of devices are shown in Fig. 4a, b and detailed performance parameters are listed in Table 1. The pristine PM6:Y6 FOSCs showed an efficiency of $\sim 15\%$. In the case of SEBS doping, a slight decrease of J_{SC} from 24.97 to 24.19 mA cm^{-2} was observed as SEBS doping content increased from 0% to 50%, resulting in a decrease in power conversion efficiency (PCE) from 14.83% to 14.10%. When SEBS content dramatically increased to 100%, J_{SC} significantly reduced to 22.60 mA cm^{-2} , and FF also decreased from 69.51% to 67.23%, which caused the decrease of PCE to 12.76%. Based on the above results, we can find that the reduced PCE was mainly related to the decrease of J_{SC} and FF. For the FOSCs based on SEBS-interface modification, there was no significant degradation of device performance as long as the concentration of SEBS was lower than 8 mg mL^{-1} . As increasing concentration to 12 mg mL^{-1} , increased thickness of the SEBS interface layer resulted in the decrease of FF.

As an optimized concentration of 8 mg mL^{-1} , the thickness of SEBS layer was about 5 nm as shown by the cross-sectional SEM image (Supplementary Fig. 7). Such a thin SEBS films would not influence the charge transporting. Actually, we found SEBS formed a nanodot morphology on the top active layer rather than a compact film. The device gave an open-circuit (V_{OC}) of 0.814 V, J_{SC} of 24.82 mA cm^{-2} , FF of 69.39%, and PCE of 14.13%. As mentioned above, we know the PM6:Y6:50%SEBS and PM6:Y6/SEBS (8 mg mL^{-1}) films have a strong adhesion force with MoO_3 and MoO_3/Al . Herein, we could see both PM6:Y6:50% SEBS and PM6:Y6/SEBS (8 mg mL^{-1})-based devices gave a comparable efficiency to the pristine device, thereby it is reasonable to conclude that introduction of SEBS could ensure high performance and marvelous interface adhesion although SEBS is an insulator material. The integrated J_{SC} (Fig. 4b) calculated over EQE spectra was in good agreement with the J - V characteristics.

As previously demonstrated, 50%, 100% SEBS-doping, and SEBS-interface modification provided a stronger interfacial adhesion between MoO_3 and the active layer. Similarly, the mechanical flexibility of PM6:Y6:50%SEBS/ MoO_3 , PM6:Y6:100%SEBS/ MoO_3 , and PM6:Y6/SEBS/ MoO_3 -based FOSCs was studied with outward bending direction and bending radius of 5 mm, and the results were shown in Fig. 4c and Supplementary Table 5. The undoped PM6:Y6 devices remained 83% of initial PCE after 5000 bending cycles. In comparison with the undoped devices, the FOSCs doped with SEBS showed a slightly improved tendency with the addition of SEBS content. The FOSCs with PM6:Y6:50%SEBS, PM6:Y6:100% SEBS maintained about 85% and 87% of their initial PCE. Excitingly, the PM6:Y6/SEBS/ MoO_3 FOSCs exhibited high bending resistance during bending with a radius of 5 mm. Since the device FF almost kept constant during 5000 bending cycles, the devices still maintained 95% of the initial PCE. When the bending cycles were prolonged to 10000 times, the devices maintained higher than 91% of the initial PCE, which is one of the most stable FOSCs^{19,23,26,30,31,35,37,39,50,58,70-86} (Fig. 4d and Supplementary Table 6). Meanwhile, as shown in Supplementary Table 5, the

Table 1. Photovoltaic parameters of FOSCs with SEBS doped active layers or SEBS interface modified active layer.

Device	V_{OC} (V)	J_{SC} (mA cm ⁻²)	FF (%)	PCE _{ave} (%)	PCE _{max} (%)
PM6:Y6	0.820 ± 0.001	24.97 ± 0.18	69.51 ± 0.47	14.21 ± 0.20	14.83
PM6:Y6:5%SEBS	0.827 ± 0.001	24.66 ± 0.58	69.24 ± 0.50	14.12 ± 0.45	14.83
PM6:Y6:10%SEBS	0.825 ± 0.001	24.99 ± 0.80	69.40 ± 0.59	14.30 ± 0.17	14.26
PM6:Y6:30%SEBS	0.813 ± 0.001	24.28 ± 0.29	69.94 ± 1.05	13.82 ± 0.30	14.34
PM6:Y6:50%SEBS	0.810 ± 0.001	24.19 ± 0.34	69.40 ± 0.79	13.60 ± 0.23	14.10
PM6:Y6:100%SEBS	0.812 ± 0.001	22.60 ± 0.26	67.23 ± 0.76	12.34 ± 0.23	12.76
PM6:Y6/SEBS(2 mg mL ⁻¹)	0.828 ± 0.002	25.05 ± 0.12	68.97 ± 1.36	14.21 ± 0.30	14.51
PM6:Y6/SEBS(4 mg mL ⁻¹)	0.820 ± 0.001	24.84 ± 0.17	68.98 ± 0.73	14.05 ± 0.12	14.22
PM6:Y6/SEBS(8 mg mL ⁻¹)	0.814 ± 0.001	24.82 ± 0.13	69.39 ± 0.92	14.13 ± 0.14	14.18
PM6:Y6/SEBS(12 mg mL ⁻¹)	0.818 ± 0.001	23.46 ± 0.41	49.62 ± 1.42	9.52 ± 0.35	9.96
PM6:L8-BO	0.873 ± 0.001	25.05 ± 0.47	74.09 ± 0.81	16.12 ± 0.20	16.29
PM6:L8-BO/SEBS(8 mg mL ⁻¹)	0.857 ± 0.002	24.42 ± 0.60	73.67 ± 1.16	15.89 ± 0.57	16.15

series resistance of the devices with SEBS-doping and SEBS-interface modifying had almost no increase after bending, indicating that the interface damage during bending was successfully suppressed. Subsequently, we also tried to peel the electrodes from the SEBS-involved devices through 3 M tape. It was found the performance kept unchanged (Supplementary Fig. 8). Further, the optical microscope and SEM images of the devices (Supplementary Fig. 9) only showed some small cracks in the films, and no peeling of MoO₃ and Al electrode was found. It also could be that the PM6:Y6:50%SEBS/MoO₃ and PM6:Y6/SEBS(8 mg mL⁻¹)/MoO₃ films did not have exfoliation or cracks on the surface after 1000 outward bending cycles. These results proved that the interface adhesion between MoO₃ and the active layer, and the mechanical stability of OSCs were enhanced through SEBS interface modification.

To prove the generality of SEBS modifying strategy, we also fabricated PM6:L8-BO FOSCs, which could give a higher performance. As showed by the *J-V* characteristics and performance parameters, the SEBS modified FOSCs showed an efficiency of 16.15% for the 0.64 cm² device, which was comparable to the control device and among one of the highest performances of flexible OSCs^{18,22,23,86}. The PM6:L8-BO FOSCs kept 93% of initial efficiency after 10000 bending cycles (Supplementary Fig. 10).

As mentioned above, the dramatically improved interfacial adhesion between MoO₃ and active layer had been proved by doping 50%, 100% SEBS in BHJ films or introducing SEBS as an interface layer between BHJ and MoO₃, while the improvement of bending resistance of FOSCs had a different trend. To explore the reasons for different trends caused by the two different SEBS treatment methods, atomic force microscope (AFM), grazing-incidence wide-angle X-ray scattering (GIWAXS), and transmission electron microscope (TEM) of these different films were investigated. The AFM height and phase images were shown in Supplementary Fig. 11. The PM6:Y6 binary blend film exhibited relatively uniform and well-distributed film morphologies with a root mean square (RMS) roughness of less than 1 nm (Supplementary Fig. 11a). For SEBS-doping films, the RMS roughness of blend films showed an increased tendency with the increase of SEBS doping contents (Supplementary Fig. 11b–f). The RMS roughness for 5%, 10%, 30%, 50%, and 100% doped blend films are 1.4, 2.8, 19.4, 19.3, and 19.0 nm, respectively. Obviously, the rapid increase of surface roughness was due to the increase of SEBS aggregation, which could be confirmed by previously reported work⁴⁷. As shown by AFM images, the brighter domains in height images gradually become larger and continuous with the increase of doping content, which might be due to the formation of larger SEBS aggregation. On contrary, for

SEBS-interface modified films, the surface of the SEBS-interface film showed a granular morphology (Supplementary Fig. 11g) with roughness as low as 0.6 nm, which was similar to the pure SEBS film (Supplementary Fig. 12), indicating that SEBS was successfully deposited on the active layer. In addition, SEBS formed a nanodot morphology on the top of active layer. Whatever SEBS doping or SEBS interface modification, the phase images of blend films (Supplementary Fig. 11h–m) showed enrichment of SEBS on the surface of the film. For the SEBS doped films, SEBS formed large-size enrichment and gradually formed a continuous film with the increase of SEBS doping concentration. While for the SEBS interface modification layer, the distribution of SEBS was more uniform. Based on these observations, we could make a conclusion that both in SEBS doping and SEBS interface modification cases, SEBS would enrich the surface of the organic photovoltaic layer as an interface glue.

TEM images of the SEBS doped PM6:Y6 films showed the aggregation of SEBS in the blend films (Supplementary Fig. 13). Besides, GIWAXS showed that SEBS doping doesn't affect the molecular orientation and crystalline of polymer donor and small-molecular acceptor (Supplementary Figs. 14, 15, and Supplementary Table 7). Such a film morphology with a large aggregation of SEBS and large surface roughness for the blend films would lead to poor exciton dissociation and transporting after continuous bending, consequently resulting in the decrease of J_{SC} . Though the improved interface adhesion made device FF more stable, finally only slight improvement of bending durability was observed. On the contrary, the TEM images (Supplementary Fig. 16) showed the modification of active layer by SEBS didn't impact the nano morphology of the active layer, which induced a stable J_{SC} during bending. Therefore, the SEBS interface bonding layer involved devices exhibited a significant improvement of bending durability.

Peak force quantitative nanomechanical mapping (PFQNM) was used to reveal the effect of SEBS treatment on the adhesion and elastic modulus of the films. As shown in Fig. 5a–c, the film without SEBS exhibited an interfacial adhesion of 9.38 nN. It gradually increased to 25.55 nN with the increase of SEBS doping concentration. When SEBS was deposited on the top of the active layer as an interfacial layer, the interfacial adhesion dramatically increased to 38.57 nN, exceeding 400% that of the w/o SEBS film (Fig. 5d). Meanwhile, the elastic modulus decreased from 762 MPa for the PM6:Y6 film to 459 and 470 MPa for the PM6:Y6:SEBS and PM6:Y6/SEBS films, respectively (Fig. 5e–h). Higher interfacial adhesion force and lower elastic modulus correspond to a tighter interface contact and better tensile strength, providing a better bending resistance. Therefore, the improved interfacial adhesion

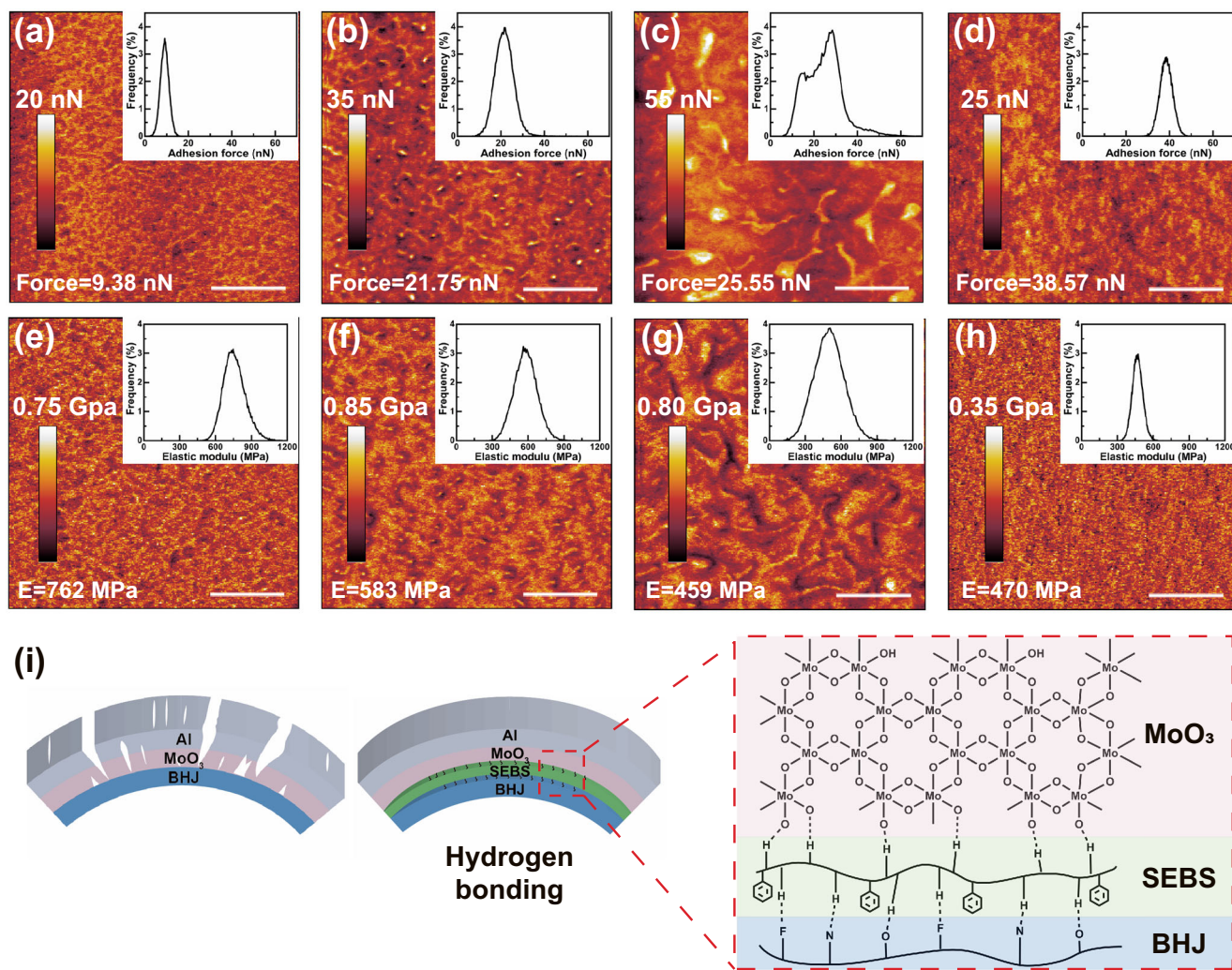


Fig. 5 Mechanism of improved bending durability of FOSCs. Adhesion images of **a** w/o SEBS (PM6:Y6), **b** 30%-SEBS doping, **c** 50%-SEBS doping, and **d** SEBS-interface films were obtained by PFQNM method (thescanned area is $2\ \mu\text{m} \times 2\ \mu\text{m}$). Elastic modulus images of **e** w/o SEBS, **f** 30%-SEBS doping, **g** 50%-SEBS doping, and **h** SEBS-interface films obtained by PFQ NM method (the scanned area is $2\ \mu\text{m} \times 2\ \mu\text{m}$). **i** Mechanism diagram of adhesion enhancement.

could be described for the following three reasons. First of all, the formation of SEBS nanodots on the surface as shown in Supplementary Fig. 12 would act as anchoring to strongly connect the active layer and MoO_3 HTL. Second, hydrogen bonds between SEBS, MoO_3 , and the active layer might be formed (Fig. 5i), which could effectively increase the interface adhesion. Besides the enhanced interface adhesion force, the existence of SEBS would also regulate the interface stress during bending. The comparison of simulated stress distribution with and without SEBS interface layer was presented in Supplementary Fig. 17. We found the stress in the central region was much higher than that of the edge region. However, the stress sharply decreased from 10^6 to $10^4\ \text{Nm}^{-2}$ after SEBS interface modification. Such a decreased stress would undoubtedly reduce the interface stress during device fabrication and bending, which also contributed to the improvement of interface bending resistance.

The operational stability of the devices during continuous illumination and thermal stability at 85°C were also monitored (Supplementary Fig. 18). It was found that both the pristine and SEBS involved devices showed $\sim 10\%$ performance degradation after 200 h continuous illumination. Similarly, these two kinds of devices showed $\sim 30\%$ degradation during thermal annealing at 85°C . These observations indicated the introduction of SEBS at

interface did not affect the operational and thermal stability of the devices.

In conclusion, the bending durability and underlying reason for performance degradation during bending for FOSCs were systematically investigated. The decrease in fill factor and efficiency of FOSCs was mainly attributed to the weak adhesion force of the organic photoactive layer and MoO_3 hole transporting layer, which caused the peel off of MoO_3 and top electrode during bending. By doping SEBS into the active layer or depositing a thin SEBS layer between MoO_3 HTL and the active layer, the adhesion between MoO_3 and the active layer is greatly improved 3–4 times. Although SEBS can protect MoO_3 during bending, large SEBS aggregates in the blend film resulted in decreasing of J_{SC} . Compared with the MoO_3 doping strategy, the SEBS interface modification strategy was more effective to improve the bending resistance due to stronger interface hydrogen bond and retentive organic layer morphology. The devices with SEBS interface modification maintained higher than 90% of the initial performance after 10000 cycles of outward bending with a radius of 5 mm. In addition, the FOSCs with SEBS interface modification gave a comparable performance of over 14% and 16% for the $0.64\ \text{cm}^2$ PM6:Y6 and PM6:L8-BO FOSCs.

METHODS

Materials

Silver nanowires dispersed in deionized water and diluted with isopropanol (IPA) were purchased from H&C Advanced Materials Ltd. The zinc acetate was supplied by Aladdin Ltd. The 2-methoxyethanol was purchased from J&K Scientific. Ethanol amine was purchased from Sigma-Aldrich. The donor PM6, acceptor Y6 and L8-BO were purchased from Solarmer Material Inc., Beijing. Chloroform (CF) was purchased from Yonghua Chemical Co. Ltd. Cyclohexane was purchased from Sinopharm Group. 1-chloronaphthalene (CN) was purchased from Sigma-Aldrich. 1,8-diiodooctane (DIO) was purchased from J&K Scientific Ltd. Hydrogenated styrene-ethylene/butylene-styrene (SEBS) block copolymer was purchased from Gainshine Co., China. Cyclohexane was purchased from Titan Scientific Co., Ltd.

Device fabrication

PET/AgNWs films are prepared by gravure printing⁵⁷. The α -ZnO layer was fabricated through sol-gel route. Typically, 0.1 M sol-gel ZnO precursor (prepared according to the literature⁸⁷) was deposited on the top of PET/AgNWs through spin-coating at 2500 rpm for 30 s. After that, the film was annealed at 150 °C for 30 min. Then, ZnO NP ETL (in CH₃OH, 15 mg mL⁻¹) was spin-coated on the top of α -ZnO film at 2500 rpm for 30 s, and the films were annealed at 130 °C for 10 min. After that, films were transferred into N₂-filled glove box to fabricate the active layer. For the SEBS doped PM6:Y6 solar cells, the active layer solution was prepared by dissolving donor PM6 and the non-fullerene acceptor Y6 in CF with a weight ratio of 1:1.2 and 0.5 vol% CN. SEBS was added in the form of SEBS solution which was dissolved in CF in advance, the content of SEBS was defined as the weight ratio of PM6. The mixed solution was stirred continuously at 50 °C overnight. Then, the mixed solution (8 mg mL⁻¹ in CF) was spin-coated on the ZnO NPs films. The active layer was annealed at 100 °C for 10 min. Finally, 20 nm MoO₃ and 150 nm Al were deposited on the active layer through vacuum evaporation. For the PM6:L8-BO solar cells, the active layer solution was prepared by dissolving donor PM6 and the non-fullerene acceptor L8-BO in CF with a weight ratio of 1:1.2 and 0.25 vol% DIO. Finally, 20 nm MoO₃ and 150 nm Al were deposited on the active layer through vacuum evaporation. For the PM6:Y6/SEBS and PM6:L8-BO/SEBS solar cells, the active layer was spin-coated on the ZnO NPs film. SEBS was pre-dissolved in cyclohexane with concentration of 2, 4, 8 and 12 mg mL⁻¹, respectively and spin-coated on the active layer. Then the film was annealed at 100 °C for 10 min. Finally, 20 nm MoO₃ and 150 nm Al were deposited on the active layer through vacuum evaporation. The area of each device is 0.64 cm².

Characterization

The current density-voltage (J - V) measurements were tested in an N₂-filled glove box with Keithley 2400 source meter under AM 1.5 G illumination (100 mWcm⁻², Zolix SS150). The SEM images were measured by S4800. XPS spectra of the remaining materials on tapes after the stripping experiment were tested by PHI 5000 Versaprobe II. AFM images of different films were tested by the Park XE-120 microscope coated with a Cr/Au conductive tip (NSC18, Mikromasch, Tallinn, Estonia.). GIWAXS images of different active layers were characterized by the Xeuss 3.0 with an X-ray wavelength of 1.341 Å (Xeuss, France). EQE spectra were characterized with a halogen lamp (Osram 64610), a monochromator (Zolix, Omni- λ 300), and a lock-in amplifier. The absorption spectra of films were tested by a Lambda 750 UV/vis/NIR spectrophotometer (PerkinElmer). The 3 M tape peeling test was carried out by pasting the 3 M tape on the top of the devices with an applied force of 6 kPa. Subsequently, the sample was put on a universal testing machine for peeling test with a peeling speed of 50 mm s⁻¹ and a peeling direction of 180°. The stress distribution in the films was studied through Finite Element Mathematical simulations.

DATA AVAILABILITY

The data that support the findings of this study are available from the corresponding author upon reasonable request.

Received: 30 March 2022; Accepted: 7 June 2022;
Published online: 07 July 2022

REFERENCES

- Kim, J. Y. et al. Leaf-inspired homeostatic cellulose biosensors. *Sci. Adv.* **7**, eabe7432 (2021).
- Zheng, S. et al. Moisture-wicking, Breathable and intrinsically antibacterial electronic skin based on dual gradient poly(ionic liquid) nanofiber membranes. *Adv. Mater.* **34**, 2106570 (2022).
- Tian, R. M., Liu, Y. Q., Koumoto, K. & Chen, J. Body heat powers future electronic skins. *Joule* **3**, 1399–1403 (2019).
- Kim, D. et al. Body-attachable and stretchable multisensors integrated with wirelessly rechargeable energy storage devices. *Adv. Mater.* **28**, 748–756 (2016).
- Li, Y. W., Xu, G. Y., Cui, C. H. & Li, Y. F. Flexible and semitransparent organic solar cells. *Adv. Energy Mater.* **8**, 1701791 (2018).
- Song, W. et al. Crumple durable ultraflexible organic solar cells with an excellent power-per-weight performance. *Adv. Funct. Mater.* **31**, 2102694 (2021).
- Sumaiya, S., Kardel, K. & El Shahat, A. Organic solar cell by inkjet printing - an overview. 2017 *Ieee Smartworld, Ubiquitous Intell. Comput., Adv. Trusted Computed, Scalable Comput. Commun., Cloud Big Data Comput., Internet People Smart City Innov.* **5**, 53 (2017).
- Park, S. Y., Labanti, C., Luke, J., Chin, Y. C. & Kim, J. S. Organic bilayer photovoltaics for efficient indoor light harvesting. *Adv. Energy Mater.* **12**, 2103237 (2021).
- Cui, Y. et al. Wide-gap non-fullerene acceptor enabling high-performance organic photovoltaic cells for indoor applications. *Nat. Energy* **4**, 768–775 (2019).
- Yuan, J. et al. Single-junction organic solar cell with over 15% efficiency using fused-ring acceptor with electron-deficient core. *Joule* **3**, 1140–1151 (2019).
- Cui, Y. et al. Single-junction organic photovoltaic cells with approaching 18% efficiency. *Adv. Mater.* **32**, 1908205 (2020).
- Li, C. et al. Non-fullerene acceptors with branched side chains and improved molecular packing to exceed 18% efficiency in organic solar cells. *Nat. Energy* **6**, 605–613 (2021).
- Liu, Q. et al. 18% Efficiency organic solar cells. *Sci. Bull.* **65**, 272–275 (2020).
- Meng, H. et al. 18.77 % Efficiency organic solar cells promoted by aqueous solution processed Cobalt(III) acetate hole transporting layer. *Angew. Chem. Int. Ed.* **60**, 22554–22561 (2021).
- Lin, Y. et al. 18.4 % Organic solar cells using a high ionization energy self-assembled monolayer as hole-extraction interlayer. *ChemSusChem* **14**, 3569–3578 (2021).
- Xu, X. et al. Polymer solar cells with 18.74% efficiency: from heterojunction to interdigitated bulk heterojunction. *Adv. Funct. Mater.* **32**, 2108797 (2022).
- Guo, C. et al. Cold-aging and solvent vapor mediated aggregation control toward 18% efficiency binary organic solar cells. *Adv. Energy Mater.* **11**, 2102000 (2021).
- Liu, X. et al. Fluidic manipulating of printable zinc oxide for flexible organic solar cells. *Adv. Mater.* **34**, 2106453 (2021).
- Duan, X. et al. Ternary strategy enabling high-efficiency rigid and flexible organic solar cells with reduced non-radiative voltage loss. *Energy Environ. Sci.* **15**, 1563–1572 (2022).
- Kim, J. et al. High performance flexible transparent electrode via one-step multifunctional treatment for Ag nanonetwork composites semi-embedded in low-temperature-processed substrate for highly performed organic photovoltaics. *Adv. Energy Mater.* **10**, 1903919 (2020).
- Koo, D. et al. Flexible organic solar cells over 15% efficiency with polyimide-integrated graphene electrodes. *Energy* **4**, 1021–1034 (2020).
- Zhao, H. et al. Kinetics manipulation enables high-performance thick ternary organic solar cells via R2R compatible slot-die coating. *Adv. Mater.* **34**, 2105114 (2022).
- Han, Y. et al. 12.42% Monolithic 25.42 cm² flexible organic solar cells enabled by an amorphous ITO modified metal grid electrode. *Adv. Mater.* **34**, 2110276 (2022).
- Chong, K. et al. Realizing 19.05% efficiency polymer solar cells by progressively improving charge extraction and suppressing charge recombination. *Adv. Mater.* **34**, 2109516 (2022).
- Cui, Y. et al. Single-junction organic photovoltaic cell with 19% efficiency. *Adv. Mater.* **33**, 2102420 (2021).
- Qin, F. et al. 54 cm² large-area flexible organic solar modules with efficiency above 13%. *Adv. Mater.* **33**, 2103017 (2021).
- Park, S. et al. Self-powered ultra-flexible electronics via nano-grating-patterned organic photovoltaics. *Nature* **561**, 516–521 (2018).
- Jin, W. Y., Ovhal, M. M., Lee, H. B., Tyagi, B. & Kang, J. W. Scalable, All-printed photocapacitor fibers and modules based on metal-embedded flexible transparent conductive electrodes for self-charging wearable applications. *Adv. Energy Mater.* **11**, 2003509 (2021).
- Zheng, Y., Zhang, S., Tok, J. B. & Bao, Z. Molecular design of stretchable polymer semiconductors: current progress and future directions. *J. Am. Chem. Soc.* **144**, 4699–4715 (2022).
- Sun, Y. N. et al. Flexible organic photovoltaics based on water-processed silver nanowire electrodes. *Nat. Electron.* **2**, 513–520 (2019).

31. Sun, Y. N. et al. Flexible high-performance and solution-processed organic photovoltaics with robust mechanical stability. *Adv. Funct. Mater.* **31**, 2010000 (2021).
32. Qu, T. Y. et al. Biomimetic electrodes for flexible organic solar cells with efficiencies over 16%. *Adv. Opt. Mater.* **8**, 2000669 (2020).
33. Wageh, S. et al. Digital printing of a novel electrode for stable flexible organic solar cells with a power conversion efficiency of 8.5%. *Sci. Rep.* **11**, 14212 (2021).
34. Raman, V., Jo, J. & Kim, H. K. ITO and graphene-covered Ag grids embedded in PET substrate by thermal roll imprinting for flexible organic solar cells. *Mater. Sci. Semicond. Process.* **120**, 105277 (2020).
35. Koppitz, M., Wegner, E., Rodlmeier, T. & Colsmann, A. Hot-pressed hybrid electrodes comprising silver nanowires and conductive polymers for mechanically robust, all-doctor-bladed semitransparent organic solar cells. *Energy Technol.* **6**, 1275–1282 (2018).
36. Wang, B. Y., Lee, E. S., Oh, Y. J. & Kang, H. W. A silver nanowire mesh overcoated protection layer with graphene oxide as a transparent electrode for flexible organic solar cells. *RSC Adv.* **7**, 52914–52922 (2017).
37. Tang, H. et al. Highly conducting MXene-silver nanowire transparent electrodes for flexible organic solar cells. *ACS Appl. Mater. Interfaces* **11**, 25330–25337 (2019).
38. Wen, P. et al. A simple and effective method via PH1000 modified Ag-Nanowires electrode enable efficient flexible nonfullerene organic solar cells. *Org. Electron.* **94**, 106172 (2021).
39. Seo, J. H. et al. Cold isostatic-pressured silver nanowire electrodes for flexible organic solar cells via room-temperature processes. *Adv. Mater.* **29**, 1701479 (2017).
40. Yu, S. et al. Engineering an interfacial interaction to assist transfer printing of active layers for curved organic solar cells. *Org. Electron.* **93**, 106162 (2021).
41. Qin, F. et al. Robust metal ion-chelated polymer interfacial layer for ultraflexible non-fullerene organic solar cells. *Nat. Commun.* **11**, 4508 (2020).
42. Tan, L. et al. Highly efficient flexible polymer solar cells with robust mechanical stability. *Adv. Sci.* **6**, 1801180 (2019).
43. Chen, X. et al. Realizing ultrahigh mechanical flexibility and >15% efficiency of flexible organic solar cells via a “welding” flexible transparent electrode. *Adv. Mater.* **32**, 1908478 (2020).
44. Han, J. H. et al. A universal method to enhance flexibility and stability of organic solar cells by constructing insulating matrices in active layers. *Adv. Funct. Mater.* **30**, 2003654 (2020).
45. Han, J. et al. Identifying tunneling effects of poly(aryl ether) matrices and boosting the efficiency, stability, and stretchability of organic solar cells. *Cell Rep. Phys. Sci.* **2**, 100408 (2021).
46. Ge, Y. et al. Polyolefin elastomer as the anode interfacial layer for improved mechanical and air stabilities in nonfullerene solar cells. *ACS Appl. Mater. Interfaces* **12**, 10706–10716 (2020).
47. Peng, Z. et al. Thermoplastic elastomer tunes phase structure and promotes stretchability of high-efficiency organic solar cells. *Adv. Mater.* **33**, 2106732 (2021).
48. Wang, J. X. et al. Overlapping fasten packing enables efficient dual-donor ternary organic solar cells with super stretchability. *Energy Environ. Sci.* **14**, 5968–5978 (2021).
49. Balar, N. et al. The Importance of entanglements in optimizing the mechanical and electrical performance of all-polymer solar cells. *Chem. Mater.* **31**, 5124–5132 (2019).
50. Xie, C. C. et al. Mechanical robust flexible single-component organic solar cells. *Small Methods* **5**, 2100481 (2021).
51. Wang, Y. L. et al. Sequential blade-coated acceptor and donor enables simultaneous enhancement of efficiency, stability, and mechanical properties for organic solar cells. *Adv. Energy Mater.* **10**, 1903609 (2020).
52. Kim, Y. et al. Inverted layer-by-layer fabrication of an ultraflexible and transparent Ag nanowire/conductive polymer composite electrode for use in high-performance organic solar cells. *Adv. Funct. Mater.* **25**, 4580–4589 (2015).
53. Lan, S., Shin, H. I. & Kim, H. K. Electrically stable Ag nanowire network anodes densely passivated by a conductive amorphous InSnTiO layer for flexible organic photovoltaics. *Appl. Phys. Lett.* **117**, 123303 (2020).
54. Wang, T., Liu, J. Q. & Hao, X. T. Recent progress of organic solar cells with insulating polymers. *Sol. RRL* **4**, 2000539 (2020).
55. Liu, C. et al. Insulating polymers as additives to bulk-heterojunction organic solar cells: the effect of miscibility. *Chemphyschem* **23**, 202100725 (2022).
56. Liang, G. J., Zhu, J. X., Chen, A., Yang, Q. & Zhi, C. Y. Adhesive and cohesive force matters in deformable batteries. *npj Flex. Electron.* **5**, 27 (2021).
57. Wang, Z. et al. High power conversion efficiency of 13.61% for 1 cm² flexible polymer solar cells based on patternable and mass-producible gravure-printed silver nanowire electrodes. *Adv. Funct. Mater.* **31**, 2007276 (2020).
58. Pan, W. et al. An efficiency of 14.29% and 13.08% for 1 cm² and 4 cm² flexible organic solar cells enabled by sol-gel ZnO and ZnO nanoparticle bilayer electron transporting layers. *J. Mater. Chem. A* **9**, 16889–16897 (2021).
59. Cui, N. et al. Stretchable transparent electrodes for conformable wearable organic photovoltaic devices. *npj Flex. Electron.* **5**, 31 (2021).
60. Yang, F., Huang, Y. T., Li, Y. W. & Li, Y. F. Large-area flexible organic solar cells. *npj Flex. Electron.* **5**, 30 (2021).
61. Nickel, F. et al. Mechanically robust, ITO-free, 4.8% efficient, all-solution processed organic solar cells on flexible PET foil. *Sol. Energy Mater. Sol. Cells* **130**, 317–321 (2014).
62. Lewis, J. Material challenge for flexible organic devices. *Mater. Today* **9**, 38–45 (2006).
63. Park, S. et al. Effect of vacuum treatment in diketopyrrolopyrrole (DPP) based copolymer with ratio controlled toluene- and benzene- functional groups for efficient organic photovoltaic cells: Morphological and electrical contribution. *Org. Electron.* **46**, 183–191 (2017).
64. Yang, X. Q. et al. Ultrathin, stretchable, and breathable epidermal electronics based on a facile bubble blowing method. *Adv. Electron. Mater.* **6**, 2000306 (2020).
65. Zhou, B. Z. et al. A highly stretchable and sensitive strain sensor based on dopamine modified electrospun SEBS fibers and MWCNTs with carboxylation. *Adv. Electron. Mater.* **7**, 2100233 (2021).
66. Li, Y. et al. Mechanically interlocked stretchable nanofibers for multifunctional wearable triboelectric nanogenerator. *Nano Energy* **78**, 105358 (2020).
67. Xu, J. et al. Highly stretchable polymer semiconductor films through the nanoconfinement effect. *Science* **355**, 59–64 (2017).
68. Xian, Y. & Kang, Z. Effect of nanostructures on enhanced metal-polymer adhesion via “bottom up” strategy: a comparative study from 0 dimension to 3 dimension materials. *Mater. Sci. Eng. B* **270** (2021).
69. Tian, Y. et al. Durable and room-temperature curable superhydrophobic composite coating on nitrocellulose lacquer. *Surf. Coat. Technol.* **328**, 444–450 (2017).
70. Xie, C. et al. Miscibility-controlled mechanical and photovoltaic properties in double-cable conjugated polymer/insulating polymer composites. *Macromolecules* **55**, 322–330 (2021).
71. Seo, J. H. et al. Low-temperature solution-processed flexible organic solar cells with PFN/AgNWs cathode. *Nano Energy* **16**, 122–129 (2015).
72. Shin, D. H., Seo, S. W., Kim, J. M., Lee, H. S. & Choi, S.-H. Graphene transparent conductive electrodes doped with graphene quantum dots-mixed silver nanowires for highly-flexible organic solar cells. *J. Alloy. Compd.* **744**, 1–6 (2018).
73. Lei, T. et al. Bendable and foldable flexible organic solar cells based on Ag nanowire films with 10.30% efficiency. *J. Mater. Chem. A* **7**, 3737–3744 (2019).
74. Dong, X. et al. Flexible nonfullerene organic solar cells based on embedded silver nanowires with an efficiency up to 11.6%. *J. Mater. Chem. A* **7**, 1989–1995 (2019).
75. Zhang, W. et al. Graphene:silver nanowire composite transparent electrode based flexible organic solar cells with 13.4% efficiency. *J. Mater. Chem. A* **7**, 22021–22028 (2019).
76. Han, Y. et al. Efficiency above 12% for 1 cm² flexible organic solar cells with Ag/Cu grid transparent conducting electrode. *Adv. Sci.* **6**, 1901490 (2019).
77. Wang, Y. et al. Top and bottom electrode optimization enabled high-performance flexible and semi-transparent organic solar cells. *Mater. Chem. Front.* **5**, 4310–4316 (2021).
78. Wang, G. et al. Synergistic optimization enables large-area flexible organic solar cells to maintain over 98% PCE of the small-area rigid devices. *Adv. Mater.* **32**, 2005153 (2020).
79. Wan, J. et al. Solution-processed transparent conducting electrodes for flexible organic solar cells with 16.61% efficiency. *Nanomicro Lett.* **13**, 44 (2021).
80. Song, W. et al. All-solution-processed metal-oxide-free flexible organic solar cells with over 10% efficiency. *Adv. Mater.* **30**, e1800075 (2018).
81. Wan, J. et al. Metal oxide-free flexible organic solar cells with 0.1 M perchloric acid sprayed polymeric anodes. *J. Mater. Chem. A* **8**, 21007–21015 (2020).
82. Fan, X. et al. High-efficiency robust organic solar cells using transfer-printed PEDOT:PSS electrodes through interface bonding engineering. *Mater. Chem. Front.* **3**, 901–908 (2019).
83. Yan, T. et al. 16.67% Rigid and 14.06% flexible organic solar cells enabled by ternary heterojunction strategy. *Adv. Mater.* **31**, 1902210 (2019).
84. Peng, R. et al. Interface bonding engineering of a transparent conductive electrode towards highly efficient and mechanically flexible ITO-free organic solar cells. *J. Mater. Chem. A* **7**, 11460–11467 (2019).
85. Wang, Y. et al. Semitransparent, non-fullerene and flexible all-plastic solar cells. *Polymer* **107**, 108–112 (2016).
86. Zeng, G. et al. Realizing 17.5% efficiency flexible organic solar cells via atomic-level chemical welding of silver nanowire electrodes. *J. Am. Chem. Soc.* **144**, 8658–8668 (2022).
87. Kang, J. C. et al. Suppression of Ag migration by low-temperature sol-gel zinc oxide in the Ag nanowires transparent electrode-based flexible perovskite solar cells. *Org. Electron.* **82**, 105714 (2020).

ACKNOWLEDGEMENTS

This work was supported by Youth Innovation Promotion Association (2019317), the National Natural Science Foundation of China (22135001), CAS-CSIRO joint project of

Chinese Academy of Sciences (121E32KYSB20190021), Vacuum Interconnected Nanotech Workstation, Suzhou Institute of Nano-Tech and Nano-Bionics of Chinese Academy of Sciences (CAS).

AUTHOR CONTRIBUTIONS

All authors contributed to the preparation of this manuscript. Z.H.X. performed most of the experiments, including fabricating the flexible organic solar cells and performing the bending durability measurement. Y.F.H. performed the cross-cut measurement and analyze the data. Y.Y.B. performed the data simulation. Xingze Chen fabricated the flexible organic solar cells. J.B.G. provided the ZnO nano-inks. L.P.Z. performed the SEM measurement. G.C. provided the AgNWs electrodes. Z.H.X, Y.F.H., and Q.L. wrote this manuscript. Q.L. conceived the original idea of this work. Q.L., T.Z., and C.Q.M. supervised the overall project and revised this manuscript. Z.H.X. and Y.F.H. contributed equally to this work.

COMPETING INTERESTS

The authors declare no conflict of interests.

ADDITIONAL INFORMATION

Supplementary information The online version contains supplementary material available at <https://doi.org/10.1038/s41528-022-00188-2>.

Correspondence and requests for materials should be addressed to Qun Luo, Ting Zhang or Chang-Qi Ma.

Reprints and permission information is available at <http://www.nature.com/reprints>

Publisher's note Springer Nature remains neutral with regard to jurisdictional claims in published maps and institutional affiliations.



Open Access This article is licensed under a Creative Commons Attribution 4.0 International License, which permits use, sharing, adaptation, distribution and reproduction in any medium or format, as long as you give appropriate credit to the original author(s) and the source, provide a link to the Creative Commons license, and indicate if changes were made. The images or other third party material in this article are included in the article's Creative Commons license, unless indicated otherwise in a credit line to the material. If material is not included in the article's Creative Commons license and your intended use is not permitted by statutory regulation or exceeds the permitted use, you will need to obtain permission directly from the copyright holder. To view a copy of this license, visit <http://creativecommons.org/licenses/by/4.0/>.

© The Author(s) 2022